ADVANCED THEORY AND SIMULATIONS
www.advtheorysimul.com

Analytical Physical Model for Electrolyte Gated Organic Field Effect Transistors in the Helmholtz Approximation

*Larissa Huetter, Adrica Kyndiah, and Gabriel Gomila**

The analytical physical modeling of undoped electrolyte gated organic field effect transistors (EGOFETs) in the Helmholtz approximation is presented. A compact analytical model for the current–voltage (*I*–*V*) characteristics, which includes the effects of the access series resistance, has been derived and validated by means of 2D finite element numerical calculations. The model describes all operating regimes continuously (subthreshold, linear, and saturation regimes), covers channel lengths down to a few micrometres and only includes physical device parameters. From the model, analytical expressions have been proposed for all the phenomenological parameters (e.g., capacitance, threshold voltage, sub-threshold slope voltage, and sub-threshold capacitance) appearing in the commonly used ideal FET model. The derived analytical physical model provides a simple and quantitative way to analyze the electrical characteristics of EGOFETs and EGOFET biosensors beyond the use of the oversimplified and phenomenological ideal FET model.

1. Introduction

Electrolyte-gated organic field-effect transistors (EGOFETs)[1,2] offer great potential in the field of biosensing and bioelectronics. On the one side, the biocompatibility and soft mechanical properties of organic materials, together with their stability in an aqueous environment, make them ideal for interfacing with biological systems. On the other side, EGOFETs can be processed with cost-effective solution processing techniques without the need for complicated fabrication processes. In EGOFETs the traditional solid dielectric is replaced by an electrolyte solution that is in contact with both the gate electrode and the semiconductor film (**Figure 1**a), which is impermeable to the penetration of ions. Applying a potential to the gate electrode V_{GS} leads to the formation of electrical double layers (EDLs) at the gate/electrolyte and semiconductor/electrolyte interfaces. This process induces the injection and accumulation of charges at the surface of the semiconductor film, forming a conduction channel, whose conductivity can be modulated by the gate voltage (Figure 1b). The application of a source–drain voltage V_{DS} leads to a source–drain current I_{DS} flow, whose magnitude can also be modulated by the gate voltage. The high capacitance of the EDLs provides a strong capacitive coupling between the gate and the semiconductor, allowing low voltage (<1 V) operation and fast switching speeds. The response of EGOFETs is strongly sensitive to the properties of the gate/electrolyte and semiconductor/electrolyte interfaces, what, together with their inherent biocompatibility, has fueled its use as biosensor.[3,4]

Label-free bioelectronic biochemical sensors exhibiting limits-of-detection down to the zeptomolar–attomolar level in real biofluids have been recently demonstrated.[5] This makes EGOFETs not only one of the highest performing bioelectronic sensors, but also a promising label-free single-molecule detecting technology. In these applications, the gate electrode, typically made of gold, is bio-functionalized with a bioreceptor such as antibodies or aptamers. Upon binding to a specific target molecule (antigen), the potential drop at the gate electrode induces a shift in the threshold voltage and/or capacitance of the transistor.[6–9] Alternatively, biofunctionalization of the channel of the transistor has also been explored, although its implementation is not too favorable due to the instability of the organic semiconductors.[10] The semiconductor/electrolyte interface, instead, has been used as a sensing area to record the bioelectronic signals from excitable cells such as cardiomyocytes and neurons.[11,12] The action potentials fired by the cells change the effective gate voltage of the transistor, which is directly transduced into the transistor current I_{DS}.

EGOFETs and EGOFET biosensors are usually modeled by using the ideal current–voltage (*I*–*V*) characteristics of FETs,

L. Huetter, G. Gomila
Nanoscale Bioelectric Characterization Group
Institute for Bioengineering of Catalunya
Baldiri i Reixac 15-21, Barcelona 08028, Spain
E-mail: gabriel.gomila@ub.edu
A. Kyndiah
Center for Nano Science and Technology
Instituto Italiano di Tecnologia
Via Pascoli, 70/3, Milano 20133, Italy
G. Gomila
Department of Electronics and Biomedical Engineering
University of Barcelona
Martí i Franqués 1, Barcelona 08028, Spain

The ORCID identification number(s) for the author(s) of this article can be found under https://doi.org/10.1002/adts.202200696

DOI: 10.1002/adts.202200696

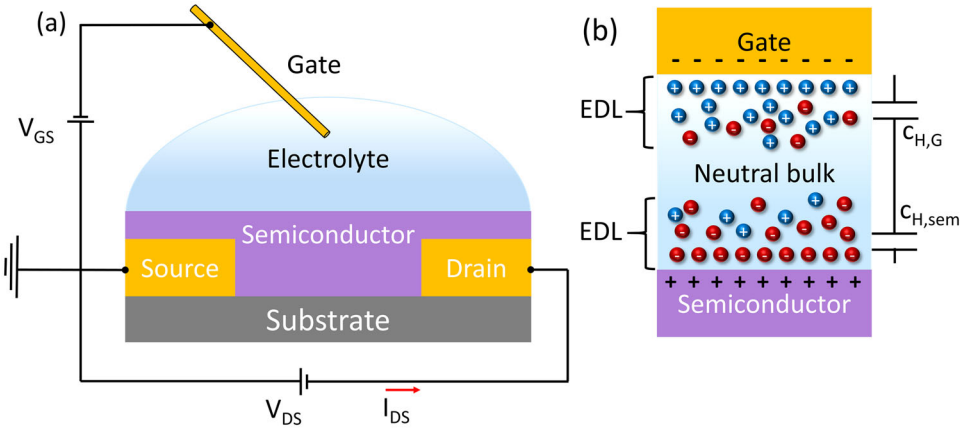

Figure 1. a) Schematic representation of an electrolyte gated organic field effect transistor (EGOFET). b) Schematic representation of the channel region with the accumulation of holes at the semiconductor surface and the electrical double layers (EDLs) represented here by Helmholtz capacitances.

which in its simplest version for a p-type semiconductor reads[13,3]

$$I_{DS} = \begin{cases} \mu_p \frac{W}{L} c_{DL} \left[-\left(V_{GS} - V_{TH}\right) V_D + \frac{1}{2} V_D^2 \right], & V_{GS} < V_{TH}, \quad V_{GS} - V_D < V_{TH} \\ -\frac{1}{2} \mu_p \frac{W}{L} c_{DL} \left(V_{GS} - V_{TH}\right)^2, & V_{GS} < V_{TH}, \quad V_{GS} - V_D > V_{TH} \\ \frac{W}{L} \mu_p c_0 V_{SS}^2 \exp\left(-\frac{V_{GS} - V_{TH}}{V_{SS}}\right) \left(\exp\left(\frac{V_{DS}}{V_{SS}}\right) - 1\right), & V_{GS} > V_{TH}, \quad V_{GS} - V_D > V_{TH} \end{cases} \tag{1}$$

This model includes adjustable phenomenological parameters such as the device double layer capacitance c_{DL}, the threshold voltage V_{TH}, the sub-threshold capacitance c_0, and the sub-threshold slope voltage V_{SS}, related to the sub-threshold slope S as $V_{SS} = S/\ln(10)$. Despite its wide use, the relationship between the phenomenological parameters and the physical device parameters is still absent. This fact has introduced some ambiguity in the interpretation of biosensing experiments.

Further insight on the physics of EGOFETs has been gained by numerically solving physical models for EGOFETs. Melzer et al.[14] modeled EGOFETs by approximating the electrolyte by a Helmholtz capacitance and numerically solved the drift-diffusion semiconductor equation. Later, Popescu et al.[15] introduced ionic diffusive effects by solving the Poisson–Boltzmann model in the electrolyte and coupling it with the Helmholtz model. Finally, Delavari et al.[16] modeled EGOFETs numerically in the Nernst-Planck–Poisson framework, coupling the ionic transport in the electrolyte with the drift-diffusion hole transport in the semiconductor. These approaches have enabled introducing different physical effects in the modeling of EGOFETs, however, they have not addressed more fundamental aspects, like the assessment of the validity of the ideal FET model for EGOFETs or the derivation of relationships linking the phenomenological FET parameters and the device physical parameters.

The present work addresses precisely these questions by developing the analytical physical modeling of EGOFETs in the Helmholtz approximation. The Helmholtz approximation is expected to be valid either when the capacitance of the interfacial compact layers is relatively small or when the ionic concentration of the electrolyte is very high. In both cases, the response is dominated by the interfacial compact layers and ionic diffusive effects can be neglected. In the Helmholtz approximation[17] the electrical double layers (EDLs) are treated as capacitors with a constant specific capacitance c_H, referred to as the Helmholtz's capacitance, and no voltage drop is assumed to take place across the electrolyte. As a result, the electrolyte in an EGOFET can be represented by two Helmholtz capacitances in series, $c_{H,G}$ and $c_{H,sem}$, corresponding, respectively, to the gate/electrolyte and semiconductor/electrolyte interfaces (Figure 1b), giving an overall equivalent Helmholtz capacitance $c_H = (c_{H,G}{}^{-1} + c_{H,sem}{}^{-1})^{-1}$. The resulting model is formally equivalent to that of an organic thin film transistor (OTFT), with c_H playing the role of the gate insulator capacitance c_i. Despite this formal similarity, a specific treatment of the problem for EGOFETs beyond the available results for OTFTs[18] is necessary. First, because the existing analytical physical models for TFTs have not worked out the relationship between the phenomenological parameters of the ideal FET model (e.g., c_{DL}, V_{TH}, c_0 or V_{SS}), and the physical device parameters (e.g., injection potential barrier, semiconductor thickness, gate-electrolyte and semiconductor-electrolyte interfacial capaci-

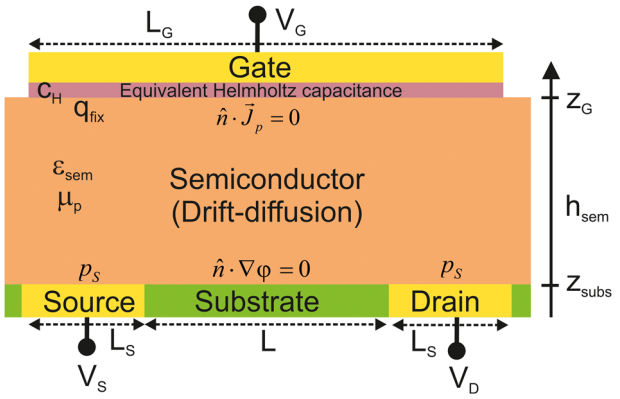

Figure 2. Schematic representation of an electrolyte gated organic field effect transistor in the Helmholtz approximation, with the physical parameters and theoretical framework used in its modeling.

tances, surface charge, etc.), which is one of the objectives of the present work, due to its relevance in EGOFET biosensing applications. And second, because a fully analytical expression for the access series resistance has not been provided,[19] which is necessary to analyze the properties of EGOFETs, which usually present a staggered configuration. Besides these facts, we note that there are important differences between OTFTs and EGOFETs in the Helmholtz approximation. On the one side, the value of c_H in EGOFETs depends on several phenomena occurring at the electrolyte interfaces, making its quantitative estimation a priori problematic, while in TFTs the capacitance c_i is well defined by the properties of the gate dielectric film. Moreover, the value of c_H in EGOFETs are usually much higher than those of c_i in TFTs (μF cm^{-2} versus tens nF cm^{-2}). Finally, the values of c_H, and other device EGOFET parameters, can vary during biosensing experiments, something that do not happen with OTFTs. We solve analytically the model and derive an analytical expression for the current–voltage characteristics, which includes the contribution of access series resistance effects. The current–voltage characteristic model reproduces the predictions of 2D finite element numerical calculations down to few micrometric-long channels. With the analytical model, we have derived closed analytical expressions for the phenomenological parameters of the ideal FET model in terms of the device's physical parameters.

2. 2D Helmholtz Model for EGOFETs and Its Approximate Analytical Solution

Figure 2 shows a schematic representation of the EGOFET model in the Helmholtz approximation analyzed in the present work. As mentioned before c_H represents the series combination of the interfacial capacitances of the gate/electrolyte and semiconductor/electrolyte interfaces.

As mentioned before, in this approximation, the device is formally equivalent to a staggered OTFT. The semiconductor is assumed to be impermeable to the penetration of ions, undoped and without traps. Moreover, it contains only one type of carriers (holes), since the source and drain electrodes are assumed to inject only one type of carriers, as it is usual in most organic devices. The injected hole carrier density at the source and drain electrodes is fixed to p_S (see below). The semiconductor film is characterized by its thickness h_{sem}, dielectric constant ϵ_{sem}, and hole mobility μ_p (assumed isotropic and field independent for simplicity). The equivalent specific capacitance c_H, which includes a fixed surface charge q_{fix}, represents the electrolyte. The free carrier transport in the semiconductor is described through the drift-diffusion model

$$-\epsilon_0\epsilon_{sem}\nabla^2\varphi = ep \tag{2}$$

$$\frac{\partial p}{\partial t} + \nabla\cdot\vec{J}_p = 0 \tag{3}$$

$$\vec{J}_p = -\mu_p p\vec{\nabla}\varphi - D_p\vec{\nabla}p \tag{4}$$

where φ is the electric potential and p the hole density. Moreover, e is the electron charge, $\vec{J}_p$ the hole number flux density and D_p the hole diffusion coefficient. This latter parameter is related to the hole mobility μ_p by Einstein's relation, which for non-degenerate semiconductors reads $D_p = \mu_p k_B T/e$, where k_B is Boltzmann's constant and T the temperature. The Helmholtz capacitance is modeled by a distributed capacitance boundary condition with zero current flux, that is,

$$\hat{n}\cdot\vec{J}_p\left(z_G^-\right) = 0 \tag{5}$$

$$\epsilon_0\epsilon_{sem}\hat{n}\cdot\vec{\nabla}\varphi\left(z_G^-\right) = -c_H\left[\varphi\left(z_G^-\right) - V_G + \Delta V_{q_{fix}}\right] \tag{6}$$

where V_G is the potential of the gate electrode and

$$\Delta V_{qfix} = q_{fix}/c_H \tag{7}$$

is the gate voltage shift due to the fixed charges at the surface of the Helmholtz capacitance. Here, z_G^- indicates that the functions are evaluated on the semiconductor side of the gate-semiconductor interface. The source and drain electrodes are assumed to form ideal metal–semiconductor diffusive injecting contacts.[20,21] Therefore, the hole density p_S takes a fixed value at their surfaces, which depends on the metal–semiconductor barrier height (see Appendix A):

$$p\left(z_{subs}^+\right) = p_S, \quad \text{source and drain} \tag{8}$$

Here, z_{subs}^+ indicates that the functions are evaluated on the semiconductor side of the substrate–semiconductor interface. Non-ideal hole injection effects related to thermionic emission, interfacial polarization and disorder[22] and to the presence of interfacial states[23] are neglected. In this approximation p_S is a constant independent of the applied gate voltage. At the bottom of the semiconductor film, in the channel region, we assume an insulating boundary condition, i.e.

$$\hat{n}\cdot\vec{\nabla}\varphi\left(z_{subs}^+\right) = 0, \quad \text{channel} \tag{9}$$

For simplicity, we do not consider any difference in the metal work functions of the different electrodes. This fact, together with the ideality of the injecting electrodes makes that the source–gate and source–drain voltages are simply given by $V_{GS} = V_G - V_S$ and $V_{DS} = V_D - V_S$. If a metal work function difference $\Delta\phi_m$ existed

between the gate and source electrodes (or a variation of this magnitude occurred during the biosensing process), then the value of V_{GS} (or V_{DS}) should be shifted to $V_{GS} - \Delta\phi_m$. Finally, on the sides of the semiconductor simulation domain, we assumed zero charge and zero flux boundary conditions. Equations (2)–(4) subject to the boundary conditions in Equations (5), (6), (8), and (9) constitute a complete set of equations to determine the electric potential and free hole concentration in an undoped EGOFET in the Helmholtz approximation. This model constitutes a simplified version of the Helmholtz model for EGOFETs considered in ref. [14] (here we assumed a field independent mobility and no presence of interface traps, among other differences). The width of the device W is assumed to be much larger than its length L so that the model can be solved in 2D with no variations along the width direction.

The 2D model, in general, can only be solved numerically.[14] However, in the long channel limit an analytical solution can be derived by resorting to the gradual channel and space charge limited transport approximations.[18,24] In these approximations, the electric field along the transversal direction of the semiconductor film is assumed to vary much more rapidly than along the longitudinal direction. Therefore, the longitudinal transport problem can be treated as a 1D problem, in which diffusive effects can be neglected (space charge limited transport condition). Hence, the source–drain current I_{DS} can be calculated as

$$I_{DS}\left(V_{DS}, V_{GS}\right) = -\frac{Wh_{sem}}{L}\int_0^L \sigma\left(x\right)\frac{\partial V\left(x\right)}{\partial x}\mathrm{d}x \tag{10}$$

where $\sigma(x) = \mu_p q_{sem}(x)/h_{sem}$ is the sheet semiconductor conductivity, with $q_{sem}(x)$ being the sheet accumulated charge in the semiconductor. This charge is obtained by integration of the free carrier charge along the transversal semiconductor direction. Moreover, the dependence on the source–drain voltage V_{DS} can be obtained by using the conductivity at V_{DS} =0 V $\sigma_0(V_{GS})$ and evaluating it at the corresponding local "gate" voltage, $V_{GS} - V(x)$, that is,

$$\sigma\left(x\right) = \sigma_0\left(V_{GS} - V\left(x\right)\right) \tag{11}$$

where $V(x)$ is the electric potential drop along the channel. Substitution of Equation (11) into Equation (10) leads to

$$I_{DS0}\left(V_{DS}, V_{GS}\right) = -\frac{Wh_{sem}}{L}\int_{V_{GS}}^{V_{GS}-V_{DS}} \sigma_0\left(V\right)\mathrm{d}V \tag{12}$$

Equation (12) shows that within these approximations the I–V characteristics can be determined by knowing the sheet semiconductor conductivity for V_{DS} =0 V as a function of the gate voltage $\sigma_0(V_{GS})$.

To determine $\sigma_0(V_{GS})$, we use that for V_{DS} =0 V the carrier density and electric potential distributions in the channel region are uniform in the longitudinal direction and only vary along the transversal direction. Therefore, the problem reduces to a 1D problem along the transversal direction. To pose this 1D transversal problem correctly, one needs a boundary condition for the hole concentration at the bottom of the semiconductor film in the channel. This boundary condition can be derived from the fixed hole density boundary condition at the source and drain electrodes of the 2D model (Equation (8)). Indeed, for V_{DS} =0 V there is no current flowing in the transistor, and hence the electrochemical potential of the holes is constant. This condition immediately gives (see Appendix A)

$$p\left(z^+_{subs}\right) = p_S e^{-\frac{e\left[\varphi_{subs}-V_S\right]}{k_B T}}, \quad \text{Channel} \quad V_{DS} = 0\,\text{V} \tag{13}$$

where $\varphi_{subs} = \varphi(z^+_{subs})$ is the potential at the bottom of the semiconductor film on top of the substrate. φ_{subs} is a parameter that must be determined and depends on the source–gate potential V_{GS} The resulting transversal 1D model for V_{DS} =0 V then consists of Equations (2)–(4) along the z-direction, subject to the boundary conditions in Equations (5), (6), (9) and (13). The analytical solution of this model has been obtained in Appendix A. For the electric potential across the transversal direction of the semiconductor film $\varphi(z)$ we obtain

$$\frac{e\left(\varphi\left(z\right) - V_S\right)}{k_B T} = -\ln\left\{e^{-\frac{e\left(\varphi_{subs}-V_S\right)}{k_B T}}\left(1 + \tan^2\left[\frac{\left(z - z_S\right)}{2L_{Ds}}e^{-\frac{e\left(\varphi_{subs}-V_S\right)}{2k_B T}}\right]\right)\right\} \tag{14}$$

with φ_{sub} being given by the implicit expression

$$\begin{aligned}\frac{e\left(V_{GS} - \Delta V_{qi}\right)}{k_B T} = {} & \frac{c_{sem}}{c_H}e^{-\frac{e\left(\varphi_{subs}-V_S\right)}{2k_B T}}\tan\left(-\frac{h_{sem}}{2L_{Ds}}e^{-\frac{e\left(\varphi_{subs}-V_S\right)}{2k_B T}}\right) \\ & -\ln\left[\left(e^{-\frac{e\left(\varphi_{subs}-V_S\right)}{2k_B T}}\right)^2\left(1 + \tan^2\left(\frac{h_{sem}}{2L_{Ds}}e^{-\frac{e\left(\varphi_{subs}-V_S\right)}{2k_B T}}\right)\right)\right]\end{aligned} \tag{15}$$

Here, c_{sem} and L_{Ds} are the semiconductor diffusive capacitance and Debye screening length, respectively,

$$c_{sem} = \frac{\varepsilon_0\varepsilon_{sem}}{L_{Ds}}, \quad L_{Ds} = \sqrt{\frac{k_B T\varepsilon_0\varepsilon_{sem}}{2e^2 p_s}} \tag{16}$$

The volumetric charge density in the semiconductor film $\rho_{sem}(z) = ep(z)$ is given by (see Appendix A)

$$\rho_{sem}\left(z\right) = ep_s\exp\left[-\frac{e\left(\varphi_{sem}\left(z\right) - V_S\right)}{k_B T}\right], \tag{17}$$

which from Equation (14), together with $1+\tan^2(x)=1/\cos^2(x)$, leads to

$$\rho_{sem}\left(z\right) = \frac{ep_s e^{-\frac{e\left(\varphi_{subs}-V_S\right)}{k_B T}}}{\cos^2\left[\frac{\left(z-z_S\right)}{2L_{Ds}}e^{-\frac{e\left[\varphi_{subs}-V_S\right]}{2k_B T}}\right]} \tag{18}$$

Integration of Equation (18) across the semiconductor film gives the sheet charge accumulated in the semiconductor

$$q_{\mathrm{sem}} = c_{\mathrm{sem}} e^{-\frac{e(\varphi_{\mathrm{subs}}-V_{\mathrm{S}})}{2k_{\mathrm{B}}T}} \frac{k_{\mathrm{B}}T}{e} \tan\left(\frac{h_{\mathrm{sem}}}{2L_{\mathrm{Ds}}} e^{-\frac{e(\varphi_{\mathrm{subs}}-V_{\mathrm{S}})}{2k_{\mathrm{B}}T}}\right) \tag{19}$$

Finally, the semiconductor sheet conductivity at zero source–drain voltage reads

$$\sigma_0\left(V_{\mathrm{GS}}\right) = \mu_{\mathrm{p}} \frac{c_{\mathrm{sem}}}{h_{\mathrm{sem}}} \frac{k_{\mathrm{B}}T}{e} e^{-\frac{e[\varphi_{\mathrm{subs}}(V_{\mathrm{GS}})-V_{\mathrm{S}}]}{2k_{\mathrm{B}}T}} \tan\left(\frac{h_{\mathrm{sem}}}{2L_{\mathrm{Ds}}} e^{-\frac{e[\varphi_{\mathrm{subs}}(V_{\mathrm{GS}})-V_{\mathrm{S}}]}{2k_{\mathrm{B}}T}}\right) \tag{20}$$

Equation (20), together with Equation (15), constitutes an exact analytical parametric expression for the sheet semiconductor conductivity for V_{DS} =0 V as a function of the source–gate voltage V_{GS}. By substituting it into Equation (12) and performing the integral, one obtains the *I–V* characteristics (see Appendix A)

$$I_{\mathrm{DS},0}\left(V_{\mathrm{DS}}, V_{\mathrm{GS}}\right) = i_{\mathrm{DS}}\left(V_{\mathrm{GS}} - V_{\mathrm{DS}}\right) - i_{\mathrm{DS}}\left(V_{\mathrm{GS}}\right) \tag{21}$$

where $i_{\mathrm{DS}}\ (V)$ is an auxiliary current parametric function given by the indefinite integral of the conductivity function,

$$i_{\mathrm{DS}}\left(V_{\mathrm{GS}}\right) = \frac{1}{2}\mu_{\mathrm{p}} \frac{W}{L}\left(\frac{k_{\mathrm{B}}T}{e}\right)^2 c_{\mathrm{sem}}\left[\frac{c_{\mathrm{sem}}}{c_H} e^{-\frac{e(\varphi_{\mathrm{subs}}-V_{\mathrm{S}})}{k_{\mathrm{B}}T}} \tan^2\left(\frac{h_{\mathrm{sem}}}{2L_{\mathrm{Ds}}} e^{-\frac{e(\varphi_{\mathrm{subs}}-V_{\mathrm{S}})}{2k_{\mathrm{B}}T}}\right) - \frac{h_{\mathrm{sem}}}{L_{\mathrm{Ds}}} e^{-\frac{e(\varphi_{\mathrm{subs}}-V_{\mathrm{S}})}{k_{\mathrm{B}}T}} + 4e^{-\frac{e(\varphi_{\mathrm{subs}}-V_{\mathrm{S}})}{2k_{\mathrm{B}}T}} \tan\left(\frac{h_{\mathrm{sem}}}{2L_{\mathrm{Ds}}} e^{-\frac{e(\varphi_{\mathrm{subs}}-V_{\mathrm{S}})}{2k_{\mathrm{B}}T}}\right)\right] \tag{22}$$

The dependence of the current on V_{GS} takes place through φ_{sub}, which is determined by Equation (15). Equation (21), together with Equations (22) and (15), then constitute an exact analytical parametric expression for the *I–V* characteristics of an undoped EGOFET in the Helmholtz and gradual channel approximations. The most relevant aspect of this solution, besides its relative simplicity, is that it only involves physical device parameters.

One can write down also explicit analytical (approximate) expressions by making use of Lambert's function, *W(x)*, often used in the analytical modeling of FET devices.[25] Lambert's function *W(x)* is the function that inverts the equation $W(x)e^{W(x)} = x$. Explicit very accurate expressions for it are available (see Appendix B). For the zero source–drain voltage sheet semiconductor conductivity $\sigma_0(V_{\mathrm{GS}})$ we obtain (see Appendix B)

$$\sigma_0\left(V_{\mathrm{GS}}\right) = \begin{cases} 2\frac{k_{\mathrm{B}}T}{e}\frac{\mu_{\mathrm{p}}}{h_{\mathrm{sem}}} c_{\mathrm{H}} W\left[\frac{1}{2}\frac{c_{\mathrm{sem}}}{c_{\mathrm{H}}} e^{-\frac{e\left(V_{\mathrm{GS}}-\Delta V_{q_{\mathrm{fix}}}\right)}{2k_{\mathrm{B}}T}}\right] & V_{\mathrm{GS}} - \Delta V_{q_{\mathrm{fix}}} < V_{c,\sigma} \\ e\mu_{\mathrm{p}} p_{\mathrm{S}} e^{-\frac{e\left(V_{\mathrm{GS}}-\Delta V_{q_{\mathrm{fix}}}\right)}{k_{\mathrm{B}}T}} & V_{\mathrm{GS}} - \Delta V_{q_{\mathrm{fix}}} > V_{c,\sigma} \end{cases} \tag{23}$$

Here, $V_{c,\sigma}$ is the crossover voltage between the linear and the exponential conductivity regimes given by

$$V_{c,\sigma} = -2\frac{k_{\mathrm{B}}T}{e} \ln\left(2\frac{c_{\mathrm{H}}}{c_{\mathrm{sem}}} x_{c,\sigma}\right) \tag{24}$$

where $x_{c,\sigma}$ is the solution of the dimensionless equation

$$W\left(x_{c,\sigma}\right) = \frac{c_H}{c_{\mathrm{geom}}} x_{c,\sigma}^2, \tag{25}$$

with c_{geom} being the geometrical specific capacitance of the semiconductor film

$$c_{\mathrm{geom}} = \frac{\epsilon_0 \epsilon_{\mathrm{sem}}}{h_{\mathrm{sem}}} \tag{26}$$

On the other hand, for the current auxiliary function $i_{\mathrm{DS}}(V_{\mathrm{GS}})$ one obtains

$$i_{\mathrm{DS}}\left(V_{\mathrm{GS}}\right) = \begin{cases} 2\mu_{\mathrm{p}}\frac{W}{L}\left(\frac{k_{\mathrm{B}}T}{e}\right)^2 c_{\mathrm{H}}\left\{W^2\left[\frac{1}{2}\frac{c_{\mathrm{sem}}}{c_{\mathrm{H}}} e^{-\frac{e\left(V_{\mathrm{GS}}-\Delta V_{q_{\mathrm{fix}}}\right)}{2k_{\mathrm{B}}T}}\right] + 2W\left[\frac{1}{2}\frac{c_{\mathrm{sem}}}{c_{\mathrm{H}}} e^{-\frac{e\left(V_{\mathrm{GS}}-\Delta V_{q_{\mathrm{fix}}}\right)}{2k_{\mathrm{B}}T}}\right]\right\}, & V_{\mathrm{GS}} - \Delta V_{q_{\mathrm{fix}}} < V_{\mathrm{c}}, \\ \mu_{\mathrm{p}}\frac{W}{L} h_{\mathrm{sem}} e p_{\mathrm{S}}\left(\frac{k_{\mathrm{B}}T}{e}\right) e^{-\frac{e\left(V_{\mathrm{GS}}-\Delta V_{q\mathrm{fix}}\right)q_{\mathrm{fix}}}{k_{\mathrm{B}}T}}, & V_{\mathrm{GS}} - \Delta V_{q_{\mathrm{fix}}} > V_{\mathrm{c}} \end{cases} \tag{27}$$

where V_{c} is the crossover voltage between the quadratic and the exponential current regimes, given by

$$V_{\mathrm{c}} - \Delta V q_{\mathrm{fix}} = -2\frac{k_{\mathrm{B}}T}{e} \ln\left(2\frac{c_{\mathrm{H}}}{c_{\mathrm{sem}}} x_{\mathrm{c}}\right) \tag{28}$$

where x_{c} is the solution of the dimensionless equation

$$W^2\left(x_{\mathrm{c}}\right) + 2W\left(x_{\mathrm{c}}\right) = \frac{c_{\mathrm{H}}}{c_{\mathrm{geom}}} x_{\mathrm{c}}^2 \tag{29}$$

The solution of this equation can be approximated phenomenologically by a piecewise function of the form

$$x_c = \begin{cases} a\left(\frac{c_{geom}}{c_H}\right)^b, & \frac{c_H}{c_{geom}} \geq 0.24 \\ a'\left(\frac{c_{geom}}{c_H}\right)^{b'}, & \frac{c_H}{c_{geom}} < 0.24 \end{cases} \quad (30)$$

where $a = 1.822$, $b = 0.624$, $a'' = 1.476$ and $b'' = 0.941$. Equation (27) inserted into Equation (21) provides an explicit analytical physical model for the current–voltage characteristics I_{DS} (V_{DS}, V_{GS}) of an EGOFET in the Helmholtz and gradual channel approximations.

The ideal FET model (Equation (1)) can be derived as an asymptotic approximation to the analytical solution just derived. To this end, we introduce the normalized voltage ν as

$$\nu = -\frac{e\left(V_{GS} - \Delta V_{q_{fix}}\right)}{2k_B T} - \ln\left(2\frac{c_H}{c_{sem}}\right), \quad e^{\nu} = \frac{1}{2}\frac{c_{sem}}{c_H} e^{-\frac{e\left(V_{GS}-\Delta V_{q_{fix}}\right)}{2k_B T}} \quad (31)$$

Lambert's function in terms of the normalized voltage $W(e^{\nu})$, can be approximated by a linear function of the form (see Appendix C)

$$W_{lin}(e^{\nu}) = \alpha_W \nu - \beta_W; \quad \nu_1 < \nu < \nu_2 \quad (32)$$

where $\alpha_W = 0.903$ and $\beta_W = 1.079$ are dimensionless numerical factors valid in the range of normalized voltages between $\nu_1 = 7$ and $\nu_2 = 20$, which covers most of the usual operation range of EGOFETs (if a different range is considered the numerical parameters vary slightly). Then, by substituting Equation (32) into Equation (23) one obtains for the zero voltage sheet semiconductor conductivity

$$\sigma_0\left(V_{GS}\right) \approx \begin{cases} \frac{\mu_p}{h_{sem}} c_{DL,\sigma}\left(-V_{GS} + V_{TH,\sigma}\right), & V_{TH,\sigma} < V_{GS} \\ e\mu_p p_S e^{-\frac{e\left(V_{GS}-\Delta V_{qfix}\right)}{k_B T}}, & V_{GS} - \Delta V_{q_{fix}} > V_{c,\sigma} \end{cases} \quad (33)$$

which shows the characteristic linear and exponential voltage dependences implicit in the ideal FET model. Here, the phenomenological capacitance $c_{DL,\sigma}$ and threshold voltage $V_{TH,\sigma}$ associated to the conductivity function are given in terms of the physical device parameters by

$$c_{phen,\sigma} = \alpha_W c_H, \quad V_{TH,\sigma} = \Delta V_{q_{fix}} - 2\frac{k_B T}{e}\left[\ln\left(2\frac{c_H}{c_{sem}}\right) + \frac{\beta_W}{\alpha_W}\right] \quad (34)$$

Similarly, for the auxiliary current function $i_{DS}(V_{GS})$, after substitution of Equation (32) into Equation (27), one obtains

$$i_{DS}\left(V_{GS}\right) \approx \begin{cases} i_{DS0} + \frac{1}{2}\mu_p \frac{W}{L} c_{DL}\left(V_{GS} - V_{TH}\right)^2, & V_{GS} < V_{TH} \\ \frac{W}{L}\mu_p c_0 V_{SS}^2 \exp\left(-\frac{V_{GS} - V_{TH}}{V_{SS}}\right), & V_{GS} > V_{TH} \end{cases} \quad (35)$$

which shows the quadratic and exponential voltage dependencies of the current present in the ideal FET models. Substitution of Equation (35) in Equation (21) gives the ideal FET I–V characteristics in Equation (1). Here, the phenomenological parameters c_{DL}, V_{TH}, c_0, and V_{SS} are also expressed in terms of the physical device parameters as

$$c_{DL} = \alpha_W^2 c_H, \quad V_{TH} = -2\frac{k_B T}{e}\left(\ln\left[2\frac{c_H}{c_{sem}}\right] + \frac{\beta_W - 1}{\alpha_W}\right) + \Delta V_{q_{fix}}, \quad V_{SS} = \frac{k_B T}{e}, \quad c_0 = \frac{h_{sem} e p_S}{\left(\frac{k_B T}{e}\right)} e^{-\frac{e\left(V_{TH}-\Delta V_{q_{fix}}\right)}{k_B T}} = 2\frac{c_H^2}{c_{geom}} e^{2\frac{\beta_W+1}{\alpha_W}}, \quad i_{DS0} = -2\mu_p \frac{W}{L}\left(\frac{k_B T}{e}\right)^2 c_H \quad (36)$$

Equation (36) constitutes one of the more relevant results of the present work. Note that there are slight differences between the phenomenological parameters for the zero-voltage sheet semiconductor conductivity and for the current-voltage characteristics.

3. Verification of the Analytical Solution

To verify the analytical expressions derived in the previous section, we have solved numerically the 2D Helmholtz model for an EGOFET (i.e., Equations (2)–(4) with the boundary conditions in Equations (5), (6), (8), and (9)). To this end we used the built-in modules of Transport of Diluted Species and Electrostatics from COMSOL Multiphysics 5.5, with a rectangular mesh, with a higher density of elements at the top and bottom surfaces of the semiconductor. On the other side, the analytical expressions have been evaluated with Mathcad 15. The physical device parameters used in the analysis, if not otherwise stated, are: $p_S = 6 \times 10^{15}$ cm^{-3}, $\epsilon_{sem} = 4$, $h_{sem} = 30$ nm, $c_H = 1$ μF cm^{-2}, $\mu_p = 0.034$ cm^2 V^{-1} s^{-1}, $T = 293.15$ K, $q_{fix} = 0$ C m^{-2}, $L = 60$ μm (channel length), $W/L = 500$, $L_S = 1$ μm (source and drain electrodes lengths), $L_G = L + 2L_S$ (gate length), $L_{box} = 0.1$ μm $+L_{channel}+2{\cdot}L_{electrodes}$ (simulation box).

Figure 3a,b (symbols) shows, respectively, the electric potential and hole density along the transversal z-direction of the channel at its middle position ($x = L/2$) numerically calculated with the 2D model for $V_{DS} = 0$ V and source–gate potentials V_{GS} ranging from 0.2 to −1 V. The solid continuous lines correspond to the analytical solution derived here (Equations (14) and (18), with φ_{subs} obtained numerically from Equation (15)). The inset in Figure 3a shows the values of φ_{subs} as a function of the source gate-voltage V_{GS}. The analytical solution nicely follows the results of the 2D model, thus validating the assumptions made in its derivation.

The potential and hole density profiles show the usual behavior of accumulation mode undoped FETs. When $V_{GS} - \Delta V_{q_{fix}} < -2(k_B T/e)\ln(\pi L_{Ds}/h_{sem})$ one has $\varphi_{subs} - V_S \rightarrow -2(k_B T/e)\ln(\pi L_{Ds}/h_{sem})$, and a space charge forms across the semiconductor film with a strong accumulation of holes at

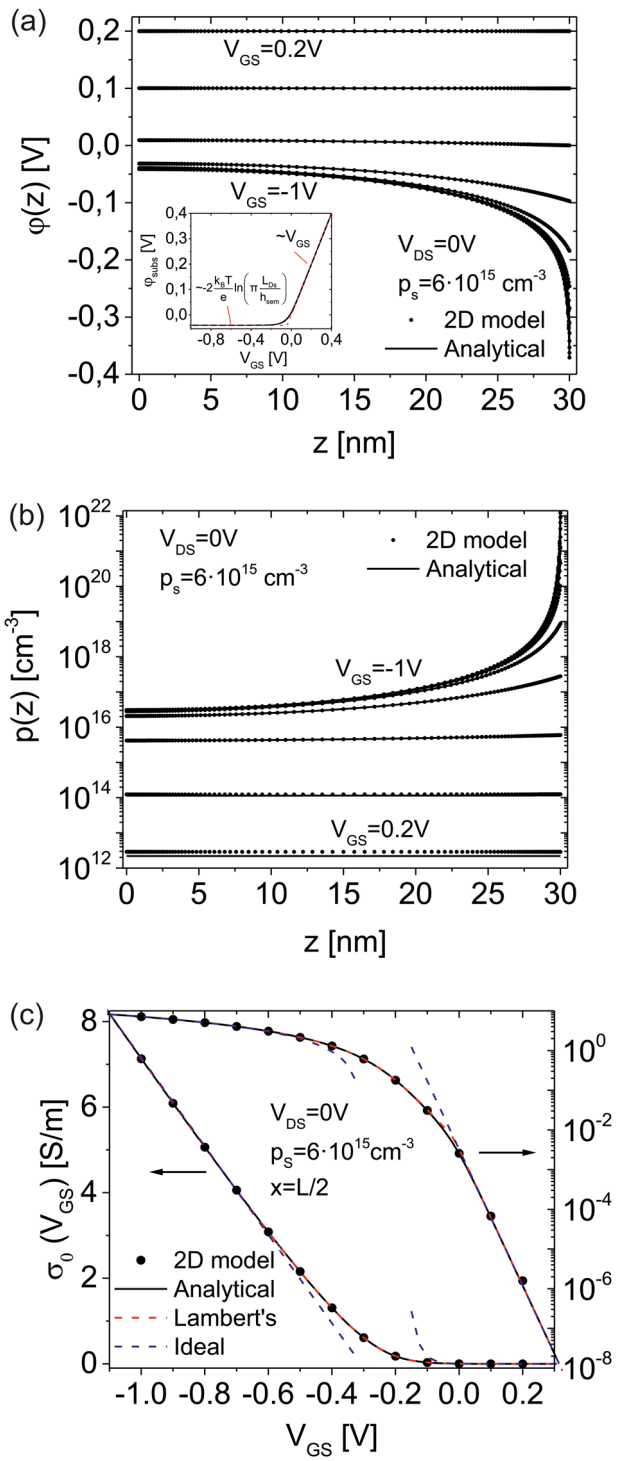

Figure 3. a,b) Electric potential and hole concentration profiles across the transversal direction of the semiconductor film at the center of the channel ($x = L/2$) for zero source–drain voltage, V_{DS} =0 V, and various source–gate potentials, V_{GS}. The symbols correspond to the 2D model numerical solution and the solid lines to the analytical solution (Equations (14) and (18), respectively, with φ_{subs} obtained numerically from Equation (15)). Inset in (a): (black line) Potential at the bottom surface of the semiconductor film, φ_{subs}, as a function of V_{GS}. The red dashed lines represent the asymptotic values of φ_{subs}. c) Sheet semiconductor conductivity σ_0 for $V_{DS} = 0$ V in the middle of the channel ($x = L/2$) for zero source–drain voltage V_{DS} = 0 V as a function of the source–gate voltage V_{GS}. As before, the symbols correspond to the 2D model and the solid black lines to the analytical solution (Equations (20) and (15)). The data are plotted in linear-linear (left axis) and log-linear (right axis) representations. The red and blue dashed lines represent, respectively, the analytical solution based on Lambert's function (Equation (23)) and the ideal FET model (Equation (33)) with the phenomenological parameters determined through Equation (34). Parameters used in the calculations: $p_S = 6 \times 10^{15}$ cm^{-3}, $\epsilon_{sem} = 4$, $h_{sem} = 30$ nm, $c_H = 1$ μF cm^{-2}, $T = 298$ K, and $q_{fix} = 0$ C m^{-2}, $L = 60$ μm, $L_S = L_D = 1$ μm, $L_{simulation,box} = 0.1$ μm + L+ L_S+ L_D, $T = 293.15$ K.

its upper surface, forming the surface conduction channel. Instead, when $V_{GS} - \Delta V_{q_{fix}} > -2(k_B T/e)\ln(\pi L_{Ds}/h_{sem})$ one has $\varphi_{subs} - V_S \rightarrow V_{GS} - \Delta V_{qi}$, and the hole distribution is almost uniform across the semiconductor film, with a value decreasing exponentially by increasing the source–gate voltage V_{GS}.

Figure 3c (symbols) shows the dependence of the zero source–drain voltage sheet semiconductor conductivity σ_0 in the middle of the channel ($x = L/2$) as a function of the source–gate voltage V_{GS} in linear-linear (left axis) and log-linear (right axis) representations, obtained by numerically solving the 2D model. The continuous black lines correspond to the analytical solution (Equation (20) with Equation (15)). The agreement between them is again excellent. The red dashed lines in Figure 3c correspond to the explicit analytical solution based on Lambert's function (Equation (23)), which is almost indistinguishable from the exact analytical solution, except at around the crossover voltage $V_{c,\sigma}$. The conductivity $\sigma_0(V_{GS})$ shows the characteristic behavior of FET devices with asymptotic linear and exponential dependencies on the source–gate voltage V_{GS}. The ideal FET conductivity model in Equation (33), with the phenomenological parameters given in Equation (34), correctly predicts these asymptotic behaviors (blue dashed lines in Figure 3c). Instead, the ideal FET model fails to describe the transition between the different regimes.

Figure 4a,b (symbols) shows the output and transfer (for $V_{DS} = -0.4$ V) I–V characteristics calculated by solving numerically the 2D Helmholtz model for $L = 60$ μm. The I-V curves show the characteristic features of FET devices, with the different transport regimes (i.e., sub-threshold, linear and saturation regimes). The continuous black lines correspond to the analytical model derived in the present work, i.e., Equation (21), together with Equations (22) and (15). The analytical model reproduces the results of the 2D numerical model, describing continuously the transition between the different regimes without including any phenomenological adjustable parameter.

We observe only slight deviations for the more negative source–gate voltages V_{GS}, which are due to the presence of access series resistance effects, as will be discussed below. The compact explicit I–V model based on Lambert's function (Equation (21) with Equation (27)) reproduces accurately the exact analytical model (red dashed lines in Figure 4), where only slight deviations at around the crossover voltage V_c are observed. Therefore, this explicit model constitutes a physical compact model to describe the I–V characteristics of EGOFETs in the Helmholtz approximation, with no adjustable phenomenological parameters. Finally, the ideal FET model in Equation (1), with the phenomenological parameters calculated according to Equation (36), constitutes a reasonable asymptotic approximation to the numerical results

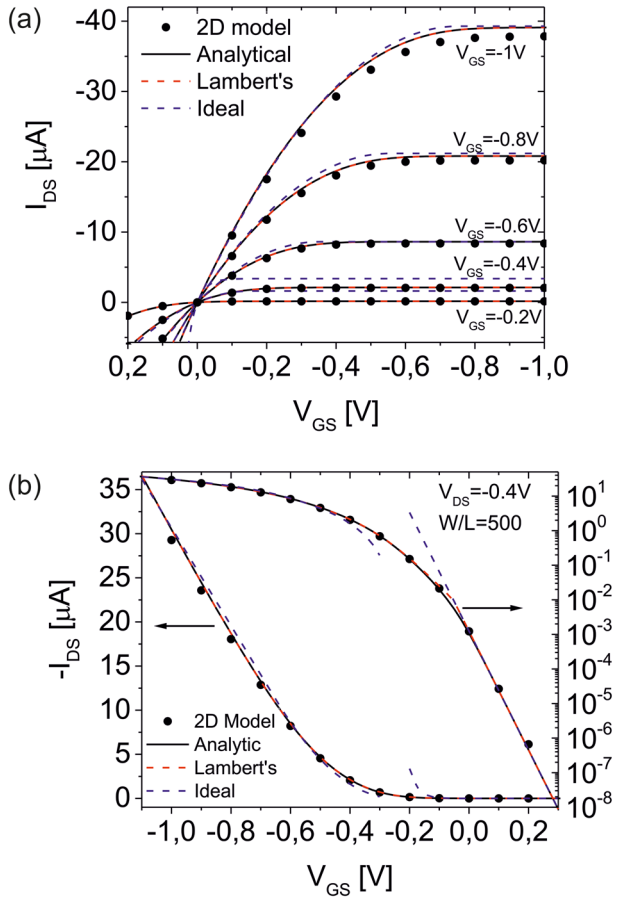

Figure 4. a,b) Output and transfer *I–V* characteristics of an EGOFET in the Helmholtz approximation. The symbols correspond to the 2D model solved numerically, the continuous lines to the analytical parametric solution (Equations (15), (21), and (22)), the red dashed lines to the explicit analytical solution based on Lambert's function (Equations (21) and (27)) and the blue dashed lines to the ideal FET model (Equation (1)) with the phenomenological parameters calculated according to Equation (36). Parameters: (same as in Figure 3) $h_{sem} = 30$ nm, $p_S = 6 \times 10^{15} cm^{-3}$, $\mu_p = 0.034\ cm^2\ V^{-1}\ s^{-1}$, $q_{fix} = 0$ V, $c_H = 10\ \mu F\ cm^{-2}$, $\epsilon_{sem} = 4$, $L_{channel} = 60$ μm, $L_{electrodes} = 1$ μm, $L_{simulation,box} = 0.1 + L_{channel} + 2L_{electrodes}$, $T = 293.15$ K, $W/L = 500$.

of the 2D Helmholtz model (blue dashed lines in Figure 4), although it shows significant deviations in the crossover between the sub-threshold and linear regimes, more evident in the transfer *I–V* curves (Figure 4b). The discontinuity in the ideal model comes from the fact that it assumes implicitly the validity of the linear dependence of the conductivity on voltage everywhere in the on state. However, there is a significant region in which the transistor is on, but the dependence is not lineal, which is the reason why one needs a more complex function to describe the dependence in this transition regime (e.g., Lambert's function). These results, on the one side, validate the use of the ideal FET model for long channel EGOFETs in the Helmholtz approximation as an asymptotic approximation. On the other side, they validate the relationships between the phenomonelogical parameters of the ideal FET model and the device's physical parameters (Equation (36)).

4. Access Series Resistance

For the highest negative source–gate voltages V_{GS} the analytical model tends to slightly overestimate the current values as compared to the predictions of the 2D model. This fact is due to the presence of access series resistance effects,[19] which are not included in the analytical solution derived so far. The access series resistance R_S accounts for the voltage drop between the injecting electrodes and the conducting channel. In the usual staggered configuration of EGOFETs, the injecting electrodes are located at the bottom of the semiconductor film, while the conducting channel is at its top surface. We derive here a fully analytical expression for R_S. To derive it, we start from the expression proposed for staggered OTFTs[19]

$$R_S = \frac{R_z}{WL_0 \tanh\left(L_{ov}/L_0\right)}, \tag{37}$$

where L_{ov} is the gate–source (or drain) overlap length. Here, R_z is the apparent resistance per unit area of the electrode region in the transversal direction, that is

$$R_z = \frac{1}{e\mu_p} \int_{z_S}^{z_S+h_{sem}} \frac{dz}{p_S(z)} \tag{38}$$

where $p_S(z)$ is the hole density distribution along the transversal direction of the semiconductor film on top of the source (or drain) electrodes. Finally, L_0 is the access length given by[19]

$$L_0 = \sqrt{\frac{R_z}{R_{sh}}} \tag{39}$$

Here, R_{sh} is the sheet resistance per unit length of the channel in the linear regime, which, according to Equation (12), is given by

$$R_{sh}\left(V_{GS}\right) = \frac{W}{L}\frac{\partial I_{DS0}}{\partial V_{DS}}\bigg|_{V_{DS}=0} = \frac{1}{\sigma_0\left(V_{GS}\right)h_{sem}} \tag{40}$$

where $\sigma_0(V_{GS})$ is given through Equation (20). To calculate the apparent electrode resistance R_z (Equation (38)) one must use the hole density distribution on top of the source or drain electrodes for V_{DS} =0 V $p_S(z)$. This density differs from the hole density distribution on the channel region $p(z)$ given in Equation (18). An exact analytical expression for $p_S(z)$ has been recently derived in the context of the analytical modeling of organic metal/insulator/semiconductor capacitors.[26] Here, we use the expression we derived in ref. [27]. From these solutions an analytical expression for R_z can be derived (see Appendix D). The derived expression for R_z can be approximated, for the calculation of the access series resistance R_S, by its value in the on-state, that is, (see Appendix D)

$$R_{z,on} = \frac{1}{2}\frac{h_{sem}}{\mu_p e p_s \beta_{max}}\left[1 - \frac{L_{Ds}}{h_{sem}\sqrt{\beta_{max}}}\sin\left(\frac{h_{sem}}{L_{Ds}}\sqrt{\beta_{max}}\right)\right] \tag{41}$$

where β_{max} is the solution of the equation

$$\begin{cases} \frac{h_{sem}}{2L_{Ds}}\sqrt{\beta_{max}} - \tan^{-1}\left(\sqrt{\frac{1}{\beta_{max}} - 1}\right) = \frac{\pi}{2}, \\ \frac{h_{sem}}{2L_{Ds}}\sqrt{\beta_{max}} + \tan^{-1}\left(\sqrt{\frac{1}{\beta_{max}} - 1}\right) = \frac{\pi}{2}, \\ \frac{h_{sem}}{L_{Dsem}}\sqrt{|\beta_{max}|} + \ln\left[\left(\sqrt{\frac{1}{|\beta_{max}|} + 1} - 1\right)\right] \Big/ \left[\left(1 + \sqrt{\frac{1}{|\beta_{max}|} + 1}\right)\right] = 0, \end{cases} \quad \begin{array}{l} p_s^* \le p_s \\ p_s^* \le p_s \le \frac{4}{\pi^2} p_s^* \\ p_s \le \frac{4}{\pi^2} p_s^* \end{array} \tag{42}$$

with

$$p_S^* = \frac{\pi^2}{2} \frac{k_B T \varepsilon_0 \varepsilon_{sem}}{e^2 h_{sem}^2} \tag{43}$$

Figure 5 (continuous line) shows the access series resistance R_S as a function of the source–gate voltage V_{GS} calculated by using Equation (37), with the help of Equations (39), (40), (20), and the exact expression for R_z given in Appendix D (Equation (D4)). The dashed line represents the calculation of R_S by approximating R_z by $R_{z,on}$ in Equation (41). Clearly, in the on-state, which is the regime of interest for series resistance considerations, the exact and the approximate expressions give identical results, so one can safely calculate R_S by using $R_{z,on}$ in Equation (41), which is much simpler to evaluate.

The series resistance R_S shows a slight dependence on V_{GS} in the on-state due to the voltage dependence of the channel resistance R_{sh}, since $R_{z,on}$ is independent from V_{GS} (see Equation (41)). With the analytical expression for R_S we analyze the effects of the different device parameters on it. Figure 5b–e shows the total access series resistance per unit of length $2R_S W$ as a function of, respectively, the injected hole density p_S, the semiconductor thickness h_{sem}, the electrode overlap length $L_{ov,}$ and the Helmholtz capacitance c_H. The total series resistance $2R_S W$ is the parameter extracted experimentally by using, for instance, the transfer length (TLM) method.[19] The parameters in Figure 5, if not otherwise stated, are those corresponding to Figure 4. The series resistance R_S is found to increase significantly when $p_S < p_S{}^*$, where $p_S{}^*$ is given in Equation (43). Additionally, it roughly increases quadratically with the semiconductor thickness h_{sem} and becomes independent from the overlap length L_{ov} above a certain critical value (here L_{ov} >1 μm), as pointed out earlier in the study of OTFTs.[19] Finally, and more significantly, the series resistance decreases when the interfacial capacitance c_H increases. Since in EGOFETs the Helmholtz capacitance c_H can take relatively large values (>1 μF cm^{-2}), access series resistance effects can be less relevant in EGOFETs than in staggered OTFTs. On the other side, since c_H can vary during biosensing experiments, R_S can also vary, making more complicate a correct interpretation of the results (see discussion).

The series resistance can be included into the analytical model for the *I–V* characteristics in a first approximation by considering the potential drop occurring at it, that is

$$I_{DS}\left(V_{DS}, V_{GS}\right) = I_{DS0}\left(V_{DS} - 2I_{DS}R_S, V_{GS} - I_{DS}R_S\right) \tag{44}$$

where $I_{DS0}(V_{DS}, V_{GS})$ is the *I–V* characteristics in the absence of series resistance effects.

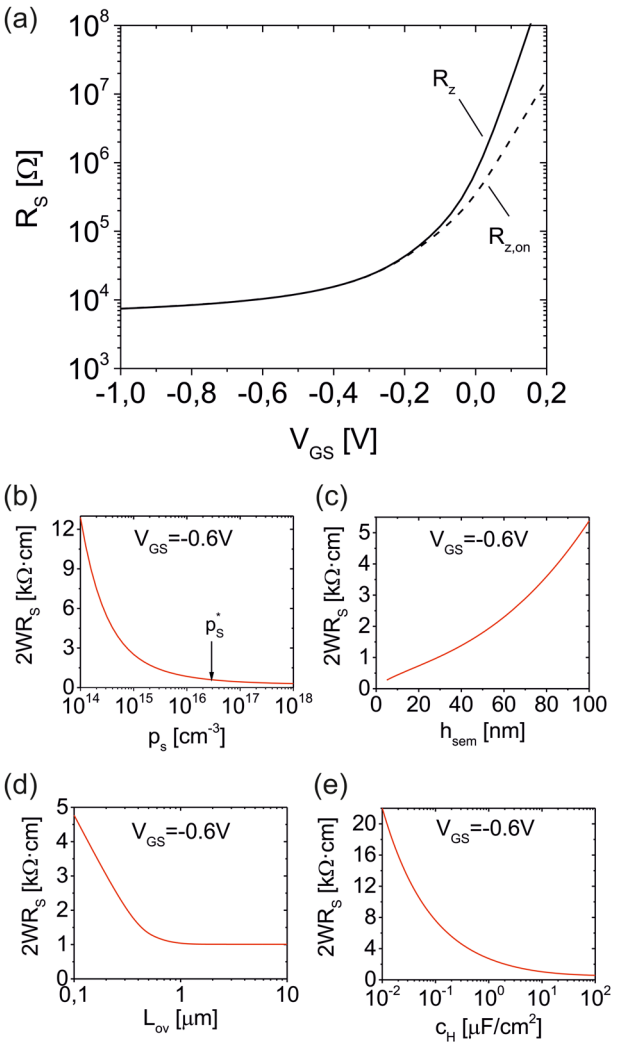

Figure 5. a) Series access resistance of the source (and drain) electrode R_S as a function of the source–gate voltage V_{GS} calculated by using Equation (37), with R_z obtained from the exact expression in Equation (D4) and from the on-state asymptotic value $R_{z,on}$ in Equation (41) (continuous and dashed lines, respectively). b–e) Total source–drain series resistance per unit of electrode width ($2WR_S$) at V_{GS} = −0.6 V as a function of the injection hole density p_S (b), thickness of the semiconductor film h_{sem} (c), overlapping electrode length L_{ov} (d), and Helmholtz capacitance c_H (e). Parameters: same as in Figure 4 if not otherwise stated.

If the potential drops are assumed to be small, one can perform a Taylor expansion of Equation (43) to obtain

$$I_{DS}\left(V_{DS}, V_{GS}\right) = \frac{I_{DS0}\left(V_{DS}, V_{GS}\right)}{1 + 2R_S g_0\left(V_{DS}, V_{GS}\right) + R_S g_{m0}\left(V_{DS}, V_{GS}\right)} \tag{45}$$

where g_0 and g_{m0} are the EGOFET conductance and transconductance in the absence of series resistance effects, respectively. These two magnitudes are directly related to the conductivity function $\sigma_0(V_{GS})$ by (see Equation (12))

$$g_0\left(V_{DS}, V_{GS}\right) = \frac{\partial I_{DS0}}{\partial V_{DS}} = \frac{Wh_{sem}}{L}\sigma_0\left(V_{GS} - V_{DS}\right) \tag{46}$$

$$g_{m0}\left(V_{DS}, V_{GS}\right) = \frac{\partial I_{DS0}}{\partial V_{GS}} = -\frac{Wh_{sem}}{L}\left[\sigma_0\left(V_{GS} - V_{DS}\right) - \sigma_0\left(V_{GS}\right)\right] \tag{47}$$

By substituting Equations (46) and (47) into Equation (45), one finally obtains the analytical physical model for the *I*–*V* characteristics of an EGOFET including access series resistance effects

$$I_{DS}\left(V_{DS}, V_{GS}\right) = \frac{I_{DS0}\left(V_{DS}, V_{GS}\right)}{1 + 2WR_S\frac{h_{sem}}{2L}\left[\sigma_0\left(V_{GS} - V_{DS}\right) + \sigma_0\left(V_{GS}\right)\right]} \tag{48}$$

In Equation (48), all terms, including R_S, can be evaluated using the analytical expressions derived in the present work, which only involve physical device parameters, and hence it does not include any adjustable phenomenological parameter.

Figure 6a,b (symbols) shows output (for $V_{GS} = -0.6$ V) and transfer (for $V_{DS} = -0.8$ V) *I*–*V* curves for an EGOFET in the Helmholtz approximation calculated numerically by solving the 2D model for different channel lengths L and fixed W/L ratio. In the absence of series resistance effects, if the ratio W/L is kept fixed the current values are independent from the channel length, L. Here, we observe a clear dependence of the current values on L, indicating the presence of access series resistance effects. For long channel lengths (here $L > 60$ µm), the effects of the series resistance become negligible and the analytical model without series resistance effects constitutes a good description of the device, as we have seen before. The analytical model including resistance effects, Equation (48), predicts reasonably well the numerical results for $L > 3$ µm, what is remarkable in view of the absence of any phenomenological adjustable parameter and the number of approximations made. We note that in the linear regime the prediction of the analytical model including series resistance effects is nearly exact, since the hypothesis made in its derivation are valid in this regime. Outside this regime the predictions turn out to be still quite accurate.

The series resistance effects can also be included in the ideal FET model by combining Equations (1), (33), and (48), giving

$$I_{DS} = \frac{\frac{W}{L}\mu_p c_{DL}\left[-\left(V_{GS} - V_{TH}\right)V_D + \frac{1}{2}V_D^2\right]}{1 + 2WR_S\frac{1}{L}\mu_p c_{DL,\sigma}\left[\left(-V_{GS} + \frac{1}{2}V_{DS} + V_{TH,\sigma}\right)\right]}, \quad \begin{matrix} V_{GS} < V_{TH} \\ V_{GS} - V_{DS} < V_{TH} \end{matrix} \tag{49}$$

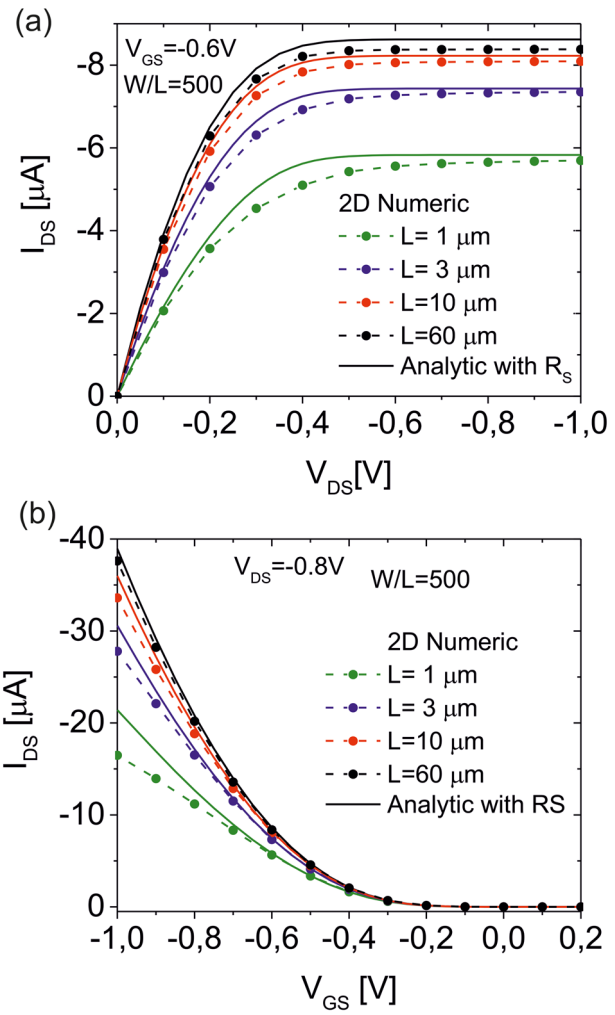

Figure 6. a) Output ($V_{GS} = -0.6$ V) and b) transfer ($V_{DS} = -0.8$ V) *I*–*V* characteristics for an EGOFET in the Helmholtz approximation calculated numerically with the 2D model for different channel lengths, L, and same W/L ratio (symbols). The continuous lines correspond to the analytical model with series resistance effects included. Note that this model has no adjustable parameter. Device parameters: same as in Figure 4.

In this expression, the phenomenological parameters, including the series resistance, are related to the physical device parameters, that is, Equations (34), (36) and (37).

5. Discussion

We have derived an analytical physical model for the *I*–*V* characteristics of undoped EGOFETs in the Helmholtz approximation (or for undoped OTFTs). This model is expected to be valid for EGOFETs with interfacial compact capacitances relatively small (<1 µF cm^{-2}) and/or electrolytes with relatively high ionic concentrations (above 100 mM), as we have shown from the analysis of organic metal-electrolyte semiconductor capacitors.[27] These conditions cover a broad range of conditions, specially for EGOFETs used as biosensors.

The model derived here, in the absence of access series resistance effects, consists of Equation (21), together with Equa-

tions (22) and (15) (an explicit expression based on Lambert's function has been also derived, given by Equations (21) and (27)). The analytical physical model involves only physical device parameters, with no phenomenological adjustable parameters. It accurately reproduces the *I*–*V* characteristics numerically calculated for 2D EGOFET models in the long channel limit. The model continuously covers all operating regimes: subthreshold, linear and saturation regimes, and it provides an accurate description of the different crossover transitions. We have shown that the ideal FET model (Equation (1)) constitutes a good asymptotic approximation to the analytical model, although it fails at the crossover regions. Expressions for the phenomenological parameters appearing in the ideal FET model in terms of the physical device parameters (Equation (36)) have been derived from the analytical physical model. These expressions are especially relevant for the threshold voltage V_{TH}, for which such expression did not exist, to our knowledge. We have found that the phenomenological device capacitance c_{DL} is proportional to the Helmholtz capacitance c_H as expected, but with a proportionality factor that slightly deviates from unity ($\alpha_W^2 \approx 0.8$). The threshold voltage V_{TH} on its side, has been found to have two main contributions (Equation (36)), namely, one related to the fixed charges at the EDLs, through the term $\Delta V_{q_{fix}}$ (Equation (7)), and one depending on the logarithm of the ratio of capacitances c_H/c_{sem}, with c_{sem} being the characteristic semiconductor diffusive capacitance (Equation (16)), which depends on the injected hole density p_S. This latter contribution can introduce significant variations in the threshold voltage V_{TH}. We show it in **Figure 7**a, where we plot V_{TH} as a function of the equivalent Helmholtz capacitance c_H for three representative injected hole densities p_S. The threshold voltage shows variations up to ±0.3 V due to this contribution, which can be relevant in the interpretation of EGOFET biosensing experiments, where c_H is one of the parameters that can vary (see below). If a work function difference existed between the different electrodes, it should also be added to the threshold voltage value, as it is well-known.

Concerning the sub-threshold regime, we have found that the sub-threshold capacitance c_0 (Equation (36)) is independent from the injected hole density p_S. Instead, c_0 is proportional to the ratio c_H^2/c_{geom}, which depends on the semiconductor film thickness. Moreover, the sub-threshold voltage V_{SS} takes the ideal thermal voltage value since the injection of carriers is assumed to be ideal. Finally, the crossover voltage between the linear and the exponential regime V_c (Equation (28)) depends logarithmically on both, the capacitance ratios c_H/c_{sem} and c_H/c_{geom}, (see Equation (30)). In Figure 7b, we show the dependence of the crossover voltage V_c as a function of the injected hole density for different Helmholtz and stray capacitances. Relatively large variations of this parameter (up to ±0.2 V) are observed depending on the physical device parameters, which can be relevant for device optimization considerations. The difference between V_c and V_{TH}, which roughly gives the crossover voltage range, is given by

$$V_{TH} - V_c = -2\frac{k_B T}{e}\left(\ln\left[x_c\right] + \frac{\beta_W + 1}{\alpha_W}\right) \quad (50)$$

This range only depends on the ratio c_H/c_{geom} through the parameter x_c, defined in Equation (29) (see also a phenomenological expression for it in Equation (30)).

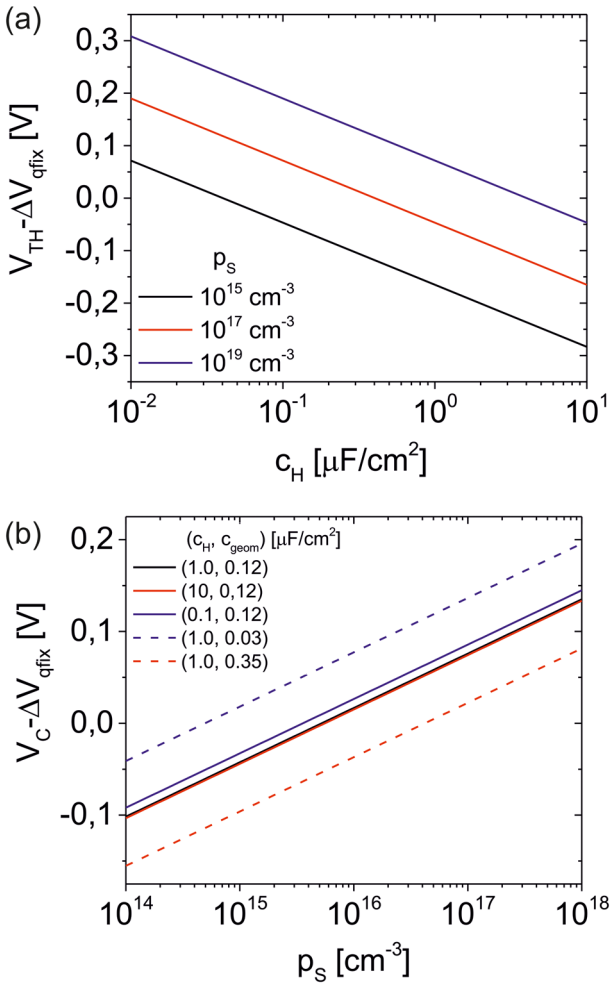

Figure 7. a) Threshold voltage V_{TH} (Equation (34)) as a function of the Helmholtz equivalent capacitance c_H for three different injected hole densities p_S. b) Crossover voltage V_c as a function of the injected hole density p_S for different values of the Helmholtz equivalent capacitance c_H and stray capacitances c_{geom} (or thicknesses of the semiconductor film). The parameters are the same as in Figure 4, if not otherwise stated.

The previous results are relevant for the physical interpretation of EGOFET biosensor experiments.[3,4] EGOFET biosensor response is usually analyzed using the ideal phenomenological FET model (Equation (1)), and parameterized through the variations of its phenomenological parameters, mainly V_{TH} and c_{DL}. With the relationships between these parameters and the physical device parameters (Equation (36)) derived here, one can further correlate the biosensor response to more fundamental physical device properties. For instance, the variation of the fixed charge of the biosensing layer q_{fix} is expected to induce a shift in the threshold voltage V_{TH} given by $\Delta V_{q_{fix}}$ in Equation (7). This shift results in the corresponding shift of the transfer *I*–*V* curves, in a similar way to the shift induced by an eventual variation of the metal work functions related to the biosensing process. On the other hand, when the biosensing process induces a modification of the thickness of the biofuntionalization layer (e.g., by the absorption of some bioanalytes), the value of the Helmholtz capacitance c_H diminishes. In this case, both the phenomenological capacitance

c_{DL} and the threshold voltage V_{TH} will vary according to Equation (36).

The variation of c_{DL} with c_H could be anticipated, but that of V_{TH} appear less obvious. As we demonstrated in Figure 7a, the variations in c_H can induce variations in V_{TH} of up to ±0.3 V, which are not related to any variation of the fixed charge or of the work functions. Finally, when modifications of both the fixed charge q_{fix} and the thickness of the biosensing layer occur, both effects add together, resulting in an overall variation of the phenomenological parameters equal to

$$\Delta c_{DL} = \alpha_W^2 \Delta c_H,$$
$$\Delta V_{TH} = \frac{q_{fix}}{c_H} - \frac{q_{fix_0}}{c_{H_0}} - 2\frac{k_B T}{e}\left(\ln\left[2\frac{c_H}{c_{H_0}}\right]\right) \quad (51)$$

This result provides a simple framework for the interpretation of EGOFET biosensing experiments in a first approximation.

When access series resistance effects play a relevant role, the situation becomes more complex. In this case, the *I–V* characteristics should be corrected to include the series resistance effects (Equation (48)), which in the linear regime can be approximated by Equation (49). The series resistance appearing in these equations is not a free adjustable parameter, but it is determined by the physical device parameters through the analytical expression in Equation (37), together with Equations (39), (40), (41) and (20). Therefore, R_S is determined by the same device physical parameters that determine the rest of phenomenological parameters in Equation (36). The analysis of the biosensing response becomes then more elaborated. For instance, when the biosensing process involves a variation of the interfacial capacitance c_H, then not only the phenomenological capacitance c_{DL} and threshold voltage V_{TH} will vary, but also the series resistance R_S itself will do (see Figure 5e). To prevent this fact, it would be desirable to design EGOFET biosensors with negligible access series resistance effects. To achieve it, one can consider different strategies by analyzing the results shown Figure 5. Alternatively, one could consider designing EGOFET biosensors enabling to track any eventual variation of the access series resistance during the biosensing process. This could be achieved, for instance, by considering multiple devices in the biosensor with different channel lengths, so that one could apply the TLM method to extract the R_S values whenever necessary. Only then the biosensing experiments could be unambiguously interpreted.

The analytical model derived here is based on a physical model that contains some approximations. These approximations render the model simple enough for a full analytical treatment. In a sense, the model offers the zeroth order approximation to a quantitative physical analysis of EGOFETs and EGOFET biosensors. Higher order approximations can be developed by relaxing some of the assumptions made and including additional effects, such as field-dependent mobilities, the presence of traps and of unintentional dopants, non-ideal hole electrode injection, disorder effects, etc. Additionally, the diffusion of the ions in the electrolyte could be explicitly included into the model[15,16] to account for the formation of the ionic diffusive space charge layers and of their voltage dependence, which are neglected in the Helmholtz approximation. Finally, the physics of the Helmholtz layers could also be modified by including ion penetration and ionic conduction effects, which could be relevant in EGOFET biosensor involving thick sensing layers that extend beyond the EDLs.[28] The analysis of these more complex physical models will inevitably lead to its resolution by means of numerical methods, since analytical solutions will be hard to be obtained. Nevertheless, the conclusions obtained with the simple model considered in the present work regarding the dependence of the phenomenological parameters on the physical device parameters are expected to remain at least qualitatively valid, and hence of broad applicability in the design and characterization of EGOFETs and EGOFET biosensors.

6. Conclusions

We have derived an analytical physical model for the *I–V* characteristics of an EGOFET in the Helmholtz approximation. The model applies continuously to all operating regimes (subthreshold, linear and saturation) and it only includes device physical parameters. The model provides an accurate description of the device in the long and short channel limits, the latter by including an analytical physical model for the access series resistance. The analytical model derived nicely reproduces the results of 2D models solved numerically. From the analytical model, we derived analytical expressions for the phenomenological parameters appearing in the ideal FET model in terms of the physical device parameters. The implications of these relationships in the design and characterization of EGOFET biosensors have been discussed and analyzed, paving the way for a more rational and quantitative interpretation and design of EGOFET biosensors.

Appendix A: Derivation of the Analytical Solution

This appendix provides the details of the derivation of the analytical solution corresponding to the 1D transversal model for V_{DS} =0 V and of the *I–V* characteristics expressions. Since the fixed charge, q_{fix}, just adds an offset to the source–gate voltage, $\Delta V_{q\,fix}$, (see Equations (6) and (7)), its effect will be added explicitly only in the final expressions after solving the problem for $q_{fix} = 0$. Under stationary conditions for $V_{DS} = 0$ V and given the zero-flux boundary condition (Equations (5)), the hole current must be null in the semiconductor, that is, $\vec{J}_p = 0$. This null current condition imply that the hole electrochemical potential is constant in space. Indeed, if we introduce the chemical potentials of the holes for non-degenerate semiconductors through the relationship

$$\tilde{\mu}_p = \tilde{\mu}_{p_S} + k_B T \ln\left(\frac{p}{p_S}\right) \quad (A1)$$

where $\tilde{\mu}_{p_S}$ is the chemical potential of reference associated to the concentration p_S, and then define the hole electrochemical potential as

$$\phi_p = \tilde{\mu}_p + e\varphi \quad (A2)$$

it is immediate to show from Equation (4) that the electrochemical potential ϕ_p is constant in space. In the semiconductor field, the chemical potentials are referred to as the Fermi levels and the electrochemical potentials as the quasi-Fermi levels. For organic semiconductors the chemical potential of holes can be defined in terms of the density of states in the semiconductor and the energy of the highest occupied molecular orbital (HOMO). In that case, instead of Equation (A1) one would write

$$\tilde{\mu}_p = \tilde{\mu}_{HOMO} + k_B T \ln\left(\frac{p}{N_{HOMO}}\right) \quad (A3)$$

from where

$$\tilde{\mu}_{p_S} = \tilde{\mu}_{HOMO} + k_B T \ln\left(\frac{p_S}{N_{HOMO}}\right) \tag{A4}$$

From Equation (A1) the hole carrier density can be written in a Boltzmann-like distribution form

$$p = p_S \exp\left(\frac{\phi_p - \tilde{\mu}_{p_S}}{k_B T}\right) e^{-\frac{e\varphi}{k_B T}} \tag{A5}$$

which by using the boundary condition in Equation (13) implies that $\phi_p = \tilde{\mu}_{p_S} - eV_S$ from where we obtain the relation

$$p = p_S e^{-\frac{e(\varphi - V_S)}{k_B T}}, \tag{A6}$$

which is valid everywhere, and in particular, at the bottom of the semiconductor film, as assumed in the boundary condition for the 1D transversal model (Equation (13)). By substituting Equation (A6) into Poisson's equation for the transverse direction (Equation (2)) one has,

$$\frac{d^2\varphi}{dz^2} = -\frac{e p_S}{\varepsilon_0 \varepsilon_{sem}} \exp\left[-\frac{e(\varphi - V_S)}{k_B T}\right], \quad z_{subs} \le z \le z_G \tag{A7}$$

As usual, a first integration of Equation (A7) can be made by multiplying these equations by the derivative of the electric potential and integrating afterwards. One obtains

$$\frac{d\varphi}{dz} = -\sqrt{\frac{2k_B T p_S}{\varepsilon_0 \varepsilon_{sem}}\left[e^{-\frac{e(\varphi - V_S)}{k_B T}} - e^{-\frac{e(\varphi_{subs} - V_S)}{k_B T}}\right]}, \quad z_{subs} \le z \le z_G \tag{A8}$$

where we used the boundary condition in Equation (9). Equation (A8) can be integrated again giving Equation (14), with L_{Ds} defined in Equation (16).

To complete the resolution of the problem one needs to determine φ_{subs}. To this end we use the boundary condition in Equation (6), with the values of the potential and its derivative at z_G obtained from Equation (14), that is

$$\frac{e(\varphi(z_G) - V_S)}{k_B T} = -\ln\left\{e^{-\frac{e(\varphi_{subs} - V_S)}{k_B T}}\left(1 + \tan^2\left[\frac{h_{sem}}{2L_{Ds}} e^{-\frac{e(\varphi_{subs} - V_S)}{2k_B T}}\right]\right)\right\} \tag{A9}$$

$$\frac{d}{dz}\left(\frac{e\varphi(z_G)}{k_B T}\right) = \frac{1}{L_{Ds}} e^{-\frac{e(\varphi_{subs} - V_S)}{2k_B T}} \tan\left[\frac{h_{sem}}{2L_{Ds}} e^{-\frac{e(\varphi_{subs} - V_S)}{2k_B T}}\right] \tag{A10}$$

One then obtains Equation (15), thus completing the derivation.

On the other hand, the diffusive boundary condition implies that the electrochemical potentials of the source electrode and of the holes are equal, that is, $\phi_p = \phi_S$, where ϕ_S is the source electrode electrochemical potential. This fact together with the non-polarizable nature of the interface implies that the injection hole chemical potential is equal to the Fermi level of the source electrode $\tilde{\mu}_{p_S} = E_{FS}$. By considering these facts, the density of injected holes is given by

$$p_S = N_{HOMO} \exp\left(-\frac{e\phi_{bp}}{k_B T}\right) \tag{A11}$$

where $e\phi_{bp} = \tilde{\mu}_{HOMO} - E_{FS}$ is the barrier height for hole injection. In a simple Mott–Schottky approximation, it is given by the difference between the hole ionization energy and the source metal work function, that is, $e\phi_{bp} = eIE_p - e\phi_{mS} = E_g - e(\phi_{mS} - \chi)$.

To derive the analytical *I–V* characteristics it is convenient to introduce the variable

$$f \equiv e^{-\frac{e(\varphi_{subs} - V_S)}{2k_B T}} \tag{A12}$$

With this variable the parametric expression of the conductivity, $\sigma_0(V_{GS})$, (Equation (20)) simply reads

$$\sigma_0(V_{GS}) = c_{sem} \frac{k_B T}{e} f \tan\left[\frac{h_{sem}}{2L_{Ds}} f\right] \tag{A13}$$

$$\frac{e\left(V_{GS} - \Delta V_{q_i}\right)}{k_B T} = -\frac{c_{sem}}{c_H} f \tan\left[\frac{h_{sem}}{2L_{Ds}} f\right] - \ln\left[f^2\left(1 + \tan^2\left[\frac{h_{sem}}{2L_{Ds}} f\right]\right)\right] \tag{A14}$$

where the parameter f is defined in the range

$$\pi \frac{L_{Ds}}{h_{sem}} < f < \exp\left[-\frac{q\left(V_{GS} - \Delta V_{q_i}\right)}{2k_B T}\right] \tag{A15}$$

The *I–V* characteristics can be obtained by substituting Equation (A13) into Equation (12) and evaluating the integral analytically. To this end, we perform the change of variable $V \to f$ for which

$$dV = -\frac{h_{sem}}{\mu_p}\frac{1}{c_H} d\sigma - \frac{k_B T}{e}\frac{2}{f} df - \frac{h_{sem}}{L_{Ds}}\frac{k_B T}{e} \tan\left[\frac{h_{sem}}{2L_{Ds}} f\right] df \tag{A16}$$

After this substitution the integral can be analytically evaluated leading to Equations (21) and (22).

Appendix B: Explicit Analytical Solution in Terms of Lambert's Function

To facilitate the evaluation and analysis of the analytical *I–V* expression derived in the previous section, we have derived an approximate, but accurate, non-parametric analytical expression based on the use of Lambert's function.[25] To derive this expression, we note that for $f \to \pi L_{Ds}/h_{sem}$ one has $\tan[h_{sem}/(2L_{Ds})f] \to +\infty$. As a result, one can neglect the unity in from of the tangent square term in Equation (A14) and approximate it by

$$\frac{e\left(V_{GS} - \Delta V_{q_{fix}}\right)}{k_B T} \approx -\frac{c_{sem}}{c_H} f \tan\left(\frac{h_{sem}}{2L_{Ds}} f\right) - \ln\left[f^2 \tan^2\left(\frac{h_{sem}}{2L_{Ds}} f\right)\right] \tag{B1}$$

This expression, with the help of the conductivity expression in Equation (A13), can be rewritten as

$$e^{\nu} = We^{W} \tag{B2}$$

where we have introduced

$$W = \frac{\sigma}{\sigma_0}; \quad \sigma_0 = 2\frac{k_B T}{e}\frac{\mu_p}{h_{sem}} c_H \tag{B3}$$

and the normalized voltage ν through Equation (31). Here, $W(e^{\nu})$ is Lambert's function, which, by definition, inverts Equation (B2).[29] An explicit

and very accurate approximate expression for Lambert's function is, for instance,[30]

$$W(x) = W_0(x)\left[1 - \frac{W_0(x) + \ln(W_0(x)) - \ln(x)}{1 + W_0(x) + \frac{W_0(x)+\ln(W_0(x))-\ln(x)}{2(1+W_0(x))}}\right] \tag{B4}$$

$$W_0(x) = \ln(1+x)\left[1 - \frac{\ln(1+x) + \ln(\ln(1+x)) - \ln(x)}{1 + \ln(1+x) + \frac{\ln(1+x)+\ln(\ln(1+x))-\ln(x)}{2(1+\ln(1+x))}}\right] \tag{B5}$$

which has an absolute accuracy better than 10^{-8} (see Appendix C).

Therefore, an explicit analytical expression for the conductivity valid in this voltage range is

$$\sigma(V_{GS}) = 2\frac{k_B T}{e}\frac{\mu_p}{h_{sem}} c_H W\left[\frac{1}{2}\frac{c_{sem}}{c_H} e^{-\frac{e\left(V_{GS}-\Delta V_{q_{fix}}\right)}{2k_B T}}\right] \tag{B6}$$

Equation (B6) is valid as long as one can neglect the unity in front of the tangent square term in Equation (A14). This condition is not satisfied in the opposite voltage limit when $f \to \exp[-q(V_{GS} - \Delta V_{q_{fix}})/(2k_B T)] << 1$. In this limit a different approximation must be used, which is based on performing a Taylor expansion of Equation (A13) to the first significant order. One obtains

$$\sigma_0(V_{GS}) \approx c_{sem}\frac{k_B T}{e}\frac{h_{sem}}{2L_{Ds}} f^2 = e\mu_p p_S e^{-\frac{e\left(V_{GS}-\Delta V_{q_{fix}}\right)}{k_B T}} \tag{B7}$$

Based on Equations (B6) and (B7), the explicit (non-parametric) analytical (approximate) expression for the zero source–drain voltage semiconductor sheet conductivity in Equation (23) is obtained. Proceeding in a similar way one arrives at the corresponding expression of the current in terms of Lambert's function in Equation (27).

Appendix C: Linear Approximation of Lambert's Function

Figure 8 (black continuos lines) shows the dependence of Lambert's function $W(e^{\nu})$ as a function of the normalized voltage ν in linear-linear and long-linear representations. The red dashed line corresponds to the approximate analytical expression in Equations (B4) and (B5). The gray line represents the linear approximation.

Appendix D: Analytical Expression for the Apparent Resistance, R_z

The hole distribution on top of the source (or drain) electrodes for V_{DS} =0 V is given by (see refs. [26] or [27])

$$p_S(z) = \frac{p_S \beta}{\cos^2\left[\mp\frac{(z-z_S)}{2L_{Ds}}\sqrt{\beta} + \tan^{-1}\left(\sqrt{\frac{1}{\beta}-1}\right)\right]}, \tag{D1}$$

where β is the solution of the equation

$$\frac{e\left(V_{GS} - \Delta V_{q_{fix}}\right)}{k_B T} = -\ln[\beta\alpha(\beta)] \mp \frac{c_{sem}}{c_{int,eq}}\sqrt{\beta[\alpha(\beta)-1]} \tag{D2}$$

with

$$\alpha(\beta) = 1 + \tan^2\left[\mp\frac{h_{sem}}{2L_{Ds}}\sqrt{\beta} + \tan^{-1}\left(\sqrt{\frac{1}{\beta}-1}\right)\right] \tag{D3}$$

For the sign convention we refer to ref. [27]. By substituting Equation (D1) into Equation (38), and performing the integral, one obtains

$$R_z = \frac{1}{2}\frac{h_{sem}}{\mu_p e p_S \beta}\left\{1 + \frac{L_{Ds}}{h_{sem}\sqrt{\beta}}\times \left[\sin\left(\frac{h_{sem}}{L_{Ds}}\sqrt{\beta} \mp 2\tan^{-1}\left(\sqrt{\frac{1}{\beta}-1}\right)\right) - \sin\left(\mp 2\tan^{-1}\left(\sqrt{\frac{1}{\beta}-1}\right)\right)\right]\right\} \tag{D4}$$

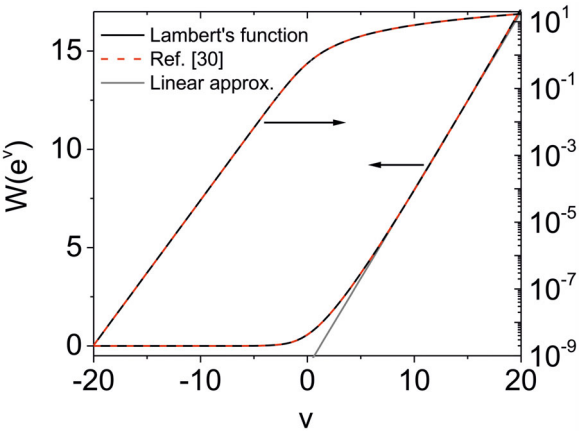

Figure 8. (Black line) Plot of Lambert's function, $W(e^{\nu})$ as a function of the normalized potential ν, represented in linear–linear (left axis) and log–linear (right axis) representations. (Red line) Explicit (approximate) expression for Lambert's function proposed in ref. [29] (Equations (B4) and (B5)). (Gray line) Linear approximation to Lambert's function in the range $7 < \nu < 20$, $W_{lin}(e^{\nu}) = \alpha_W + \beta_W$, giving $\alpha_W = 0.903$ and $\beta_W = -1.079$.

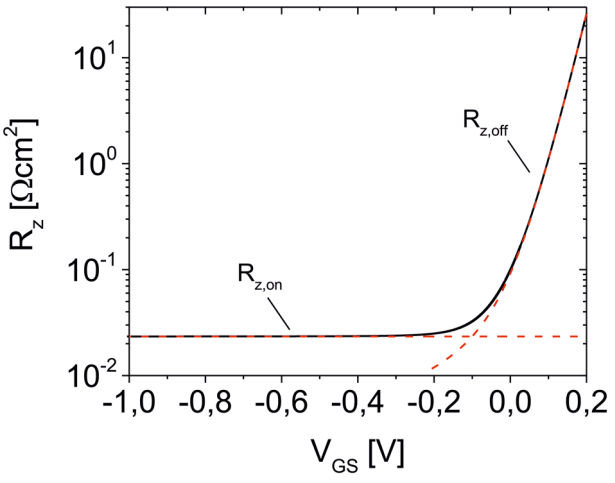

Figure 9. (Black continuous line) Apparent electrode resistance per unit of area, R_z as a function of the source gate voltage, V_{GS}, as calculated from Equation (D4). (Red dashed lines) Asymptotic values of R_z, namely, $R_{z,on}$ and $R_{z,off}$ as given in Equations (D5) and (D6), respectively. Parameters: Same as in Figure 4.

This expression gives the apparent resistance R_z in terms of V_{GS} for V_{DS} =0 V. By analyzing this expression one can show that there exist two limiting behaviors corresponding to the on and off states, that is

$$R_{z,on} = \frac{1}{2}\frac{h_{sem}}{\mu_p e p_s \beta_{max}}\left[1 - \frac{L_{Ds}}{h_{sem}\sqrt{\beta_{max}}}\sin\left(\frac{h_{sem}}{L_{Ds}}\sqrt{\beta_{max}}\right)\right] \quad \text{(D5)}$$

$$R_{z,off} = \frac{1}{\mu_p e p_s}\frac{k_B T}{eV_{GS}}\left(1 + \frac{c_{geom}}{c_H}\right)h_{sem}\left[\exp\left(\frac{eV_{GS}}{k_B T}\frac{1}{1+\frac{c_{geom}}{c_H}}\right) - 1\right] \quad \text{(D6)}$$

Figure 9 (continuous black line) shows R_z as a function of the source–gate voltage V_{GS}, as given in Equation (D4), with the values of β obtained by solving Equation (D2), for the device parameters corresponding to Figure 4. The red dashed lines in the figure correspond to the asymptotic expressions $R_{z,on}$ and $R_{z,off}$ in Equations (D5) and (D6), respectively.

Acknowledgements

L.H. and G.G. contributed equally to this work. This work had received funding from the European Union's Horizon 2020 research and innovation program under the Marie Skłodowska-Curie grant agreement No 81386 (BORGES), and from CERCA from the Generalitat de Catalunya. The authors acknowledge useful discussions with Shubham Tanwar and the members of the BORGES Marie Skłodowska-Curie ITN network.

Conflict of Interest

The authors declare no conflict of interest.

Data Availability Statement

The data that support the findings of this study are openly available in Zenodo at https://doi.org/10.5281/zenodo.7108017, reference number 7108017.

Keywords

analytical model, current–voltage characteristics, electrolyte gated organic field effect transistors

Received: September 26, 2022
Revised: January 31, 2023
Published online: February 22, 2023

[1] L. Kergoat, L. Herlogsson, D. Braga, B. Piro, M.-C. Pham, X. Crispin, M. Berggren, G. Horowitz, *Adv. Mater.* **2010**, *22*, 2565.
[2] S. H. Kim, K. Hong, W. Xie, K. H. Lee, S. Zhang, T. P. Lodge, C. D. Frisbie, *Adv. Mater.* **2013**, *25*, 1822.
[3] F. Torricelli, D. Z. Adrahtas, Z. Bao, M. Berggren, F. Biscarini, A. Bonfiglio, C. A. Bortolotti, C. D. Frisbie, E. Macchia, G. G. Malliaras, I. McCulloch, M. Moser, T.-Q. Nguyen, R. M. Owens, A. Salleo, A. Spanu, L. Torsi, *Nat. Rev. Methods Primers* **2021**, *1*, 66.
[4] D. Wang, V. Noël, P. Benoît, *Electronics* **2016**, *5*, 9.
[5] E. Macchia, K. Manoli, B. Holzer, C. Di Franco, M. Ghittorelli, F. Torricelli, D. Alberga, G. F. Mangiatordi, G. Palazzo, G. Scamarcio, L. Torsi, *Nat. Commun.* **2018**, *9*, 3223.
[6] S. Casalini, F. Leonardi, T. Cramer, F. Biscarini, *Org. Electron.* **2013**, *14*, 156.
[7] S. Casalini, A. C. Dumitru, F. Leonardi, C. A. Bortolotti, E. T. Herruzo, A. Campana, R. F. de Oliveira, T. Cramer, R. Garcia, F. Biscarini, *ACS Nano* **2015**, *9*, 5051.
[8] C. Diacci, M. Berto, M. Di Lauro, E. Bianchini, M. Pinti, D. T. Simon, F. Biscarini, C. A. Bortolotti, *Biointerphases* **2017**, *12*, 05F401.
[9] E. Macchia, R. A. Picca, K. Manoli, C. Di Franco, D. Blasi, L. Sarcina, N. Ditaranto, N. Cioffi, R. Österbacka, G. Scamarcio, F. Torricelli, L. Torsi, *Mater. Horiz.* **2020**, *7*, 999.
[10] P. Seshadri, K. Manoli, N. Schneiderhan-Marra, U. Anthes, P. Wierzchowiec, K. Bonrad, C. Di Franco, L. Torsi, *Biosens. Bioelectron.* **2018**, *104*, 113.
[11] A. Kyndiah, F. Leonardi, C. Tarantino, T. Cramer, R. Millan-Solsona, E. Garreta, N. Montserrat, M. Mas-Torrent, G. Gomila, *Biosens. Bioelectron.* **2020**, *150*, 111844.
[12] T. Cramer, B. Chelli, M. Murgia, M. Barbalinardo, E. Bystrenova, D. M. de Leeuw, F. Biscarini, *Phys. Chem. Chem. Phys.* **2013**, *15*, 3897.
[13] D. Tu, L. Herlogsson, L. Kergoat, X. Crispin, M. Berggren, R. Forchheimer, *IEEE Trans. Electron. Devices* **2011**, *58*, 3574.
[14] K. Melzer, M. Brändlein, B. Popescu, D. Popescu, P. Luglia, G. Scarpa, *Faraday Discuss.* **2014**, *174*, 399.
[15] D. Popescu, B. Popescu, M. Brändlein, K. Melzer, P. Lugli, *IEEE Trans. Electron. Devices* **2015**, *62*, 4206.
[16] N. Delavari, K. Tybrandt, M. Berggren, B. Piro, V. Noël, G. Mattana, I. Zozoulenko, *J Phys D Appl Phys* **2021**, *54*, 415101.
[17] H. Helmholtz, *Ann. Phys.* **1853**, *89*, 211.
[18] N. Lu, W. Jiang, Q. Wu, D. Geng, L. Li, M. Liu, *Micromachines* **2018**, *9*, 599.
[19] K.-D. Jung, Y. C. Kim, B.-G. Park, H. Shin, J. D. Lee, *IEEE Trans. Electron Devices* **2009**, *56*, 431.
[20] S. M. Sze, K. K. Ng, *Physics of Semiconductor Devices*, 3rd ed., John Wiley & Sons, Hoboken, NJ **2006**.
[21] G. Gomila, I. R. Cantalapiedra, L. Reggiani, *J. Appl. Phys.* **2003**, *93*, 375.
[22] S. Jung, C.-H. B. Y. Kim, G. Horowitz, *J. Phys. D: Appl. Phys.* **2015**, *48*, 395103.
[23] G. Gomila, J. M. Rubí, *J. Appl. Phys.* **1997**, *81*, 2674.
[24] W. Shockley, *Proc. IRE* **1952**, *40*, 1365.
[25] R. Chen, X. Zheng, W. Deng, Z. Wu, *Solid State Electron.* **2007**, *51*, 975.
[26] P. K. Manda, L. Karunakaran, S. Thirumala, A. Chakravorty, S. Dutta, *IEEE Trans. Electron Devices* **2019**, *66*, 3967.
[27] L. Huetter, A. Kyndiah, G. Gomila, *Adv Theory Simul* **2022**, *6*, 2200698.
[28] G. Palazzo, D. De Tullio, M. Magliulo, A. Mallardi, F. Intranuovo, Y. M. Mulla, P. Favia, I. Vikholm-Lundin, L. Torsi, *Adv. Mater.* **2015**, *27*, 911.
[29] R. Iacono, J. P. Boyd, *Adv. Comput. Math.* **2017**, *43*, 1403.
[30] J. He, M. Fang, B. Li, Y. Cao, *Solid State Electron.* **2006**, *50*, 1371.